minerals

MDPI

Article

Geochemical Characteristics of Seabed Sediments in the Xunmei Hydrothermal Field (26°S), Mid-Atlantic Ridge: Implications for Hydrothermal Activity

Peng Yang [1], Chuanshun Li [1,2,*], Yuan Dang [1,2,*], Lei Fan [1,2], Baoju Yang [3], Yili Guan [1,2], Qiukui Zhao [4] and Dewen Du [1,2]

[1] Key Laboratory of Marine Geology and Metallogeny, First Institute of Oceanography, Ministry of Natural Resources, Qingdao 266061, China; yp19981102@163.com (P.Y.); lei.fan@fio.org.cn (L.F.); guanyili@fio.org.cn (Y.G.); dwendu@fio.org.cn (D.D.)

[2] Shandong Key Laboratory of Deep Sea Mineral Resources Development, Qingdao 266061, China

[3] School of Resources and Environmental Engineering, Ludong University, Yantai 264025, China; bjyang0535@163.com

[4] College of Marine Geosciences, Ocean University of China, Qingdao 266100, China; zqk562628426@gmail.com

* Correspondence: lichuanshun@fio.org.cn (C.L.); dangyuan@fio.org.cn (Y.D.)

Abstract: The compositions of metalliferous sediments associated with hydrothermal vents can provide key geochemical data for locating seafloor sulfides. In this study, we present the geochemistry of seabed sediments from the Xunmei hydrothermal field (HF) in the South Mid-Atlantic Ridge (SMAR). The results indicate that the sediments are mainly composed of pelagic material (biogenic calcium components), basaltic debris, iron-manganese oxides, and hydrothermal components. The sediments are significantly enriched in Cu, Zn, Fe, and Co deriving from hydrothermal fluids, as well as Mn, V, Mo, U, and P, which are primarily scavenged from seawater. The northeastern Xunmei has the highest concentrations of Cu and Zn, while the northeastern, northern, and southern regions are characterized by great inputs of Fe. Manganese and Mo are mainly enriched in the western and southern parts and show a strong positive correlation, indicating that Mo is mainly scavenged by Mn oxides. Uranium, P, and Fe exhibit strong positive correlations, suggesting that they coprecipitate with Fe from hydrothermal plumes. Vanadium and Co are introduced into sediments in different ways: V is scavenged and coprecipitated by hydrothermal plumes, and Co is derived from sulfide debris. Based on the contents of Cu and Zn and Cu/Fe (0.159), Zn/Fe (0.158), and Fe/Mn (1440) ratios, it can be inferred that a high-temperature hydrothermal vent existed in northeastern Xunmei. In combination with the distribution patterns of the above elements, the hydrothermal vents in the southern part ceased erupting after a short period of activity. In addition, the high Mn anomaly and the high U/Fe ratios at the boundaries of the investigated area indicate the presence of a relatively oxidized environment in southwestern Xunmei.

Keywords: South Mid-Atlantic Ridge; metalliferous sediments; Xunmei hydrothermal field; geochemical characteristics; hydrothermal activity

Citation: Yang, P.; Li, C.; Dang, Y.; Fan, L.; Yang, B.; Guan, Y.; Zhao, Q.; Du, D. Geochemical Characteristics of Seabed Sediments in the Xunmei Hydrothermal Field (26°S), Mid-Atlantic Ridge: Implications for Hydrothermal Activity. *Minerals* **2024**, *14*, 107. https://doi.org/10.3390/min14010107

Academic Editor: Francisco J. González

Received: 24 November 2023
Revised: 8 January 2024
Accepted: 15 January 2024
Published: 19 January 2024

1. Introduction

Seafloor massive sulfide (SMS) deposits are products of submarine hydrothermal convection and are rich in metal elements such as Fe, Cu, Pb, Zn, Au, and Ag. Due to their high ore grade, shallow depth, and rapid mineralization process, SMS deposits are deep-sea mineral resources with great economic potential [1,2]. Currently, the identification of SMS deposits mainly relies on detecting plumes, which are characterized by anomalies in water turbidity, temperature, and redox potential around hydrothermal fields (HFs), and then determining the hydrothermal vents [3,4]. However, for inactive sulfide deposits, electromagnetic and magnetic methods are considered effective approaches [5]. Nevertheless, the exploration methods of sediment geochemistry for SMS deposits offer potential but still need to be improved and supplemented [6].

Metalliferous sediments are unconsolidated deep-sea deposits associated with submarine hydrothermal activity containing hydrothermal matter, terrigenous and volcanic materials, and biogenic components [7]. Compared to pelagic sediments, they are enriched in Fe, Mn, Cu, Pb, Zn, and As but depleted in Al and Ti [7–12]. The submarine sediments near HFs are frequently influenced by hydrothermal vent circulation [13]. Previous studies have identified two types of hydrothermal metalliferous sediments. The first type forms through the rapid deposition of sulfides (near a vent), which can be considered cogenetic with massive sulfides and provides a record of hydrothermal ore-forming environments [14]. The second type forms through particle settling from neutral-buoyancy hydrothermal plumes diluted by background sediments (far from a vent); this type is influenced by hydrothermal plume dispersion patterns and processes [9,13,15] and is the proxy for the presence, intensity, and location of hydrothermal vents.

Significant progress has been made in the identification of metalliferous and nonmetalliferous sediments [16,17], the geochemical characteristics of hydrothermal metalliferous sediments [12,18–20], the ore-forming environment and genesis [21,22], and the history of hydrothermal sedimentation and evolution of hydrothermal activity [23–25]. However, there is still relatively limited research on the application of sediment geochemistry in hydrothermal exploration. Previous studies have characterized the distribution of hydrothermal-derived elements in surface sediments of the TAG HF in the Mid-Atlantic Ridge [26], the Dragon Horn HF in the Southwest Indian Ocean [6], and the Duanqiao-1 HF in the Southwest Indian Ocean [27] and have discussed the relationship between element distribution and distance from the vent. The published literature indicates that relevant work in various hydrothermal fields along the South Mid-Atlantic Ridge (SMAR) has not yet been conducted.

Since 2009, investigations and studies on hydrothermal activities in the SMAR have identified several hydrothermal fields, including Xunmei, Deyin, Tongguan, and Zouyu [28–33]. Recent research indicates that non-biogenic sediments in the SMAR are primarily derived from hydrothermal sources, the second source was lithogenic components, and the third source was a number of elements scavenged from seawater [34]. However, there has been no relevant study on spatial distributions of hydrothermal components in seabed sediments. In this study, seabed sediments from 16 stations in the Xunmei HF were analyzed. We aim to explore the correlation between hydrothermal activity and element geochemistry, thereby providing a geochemical basis for the identification of unknown hydrothermal vents.

2. Geological Setting

The SMAR is divided into four segments from north to south: the Equatorial segment, the Central segment, the Austral segment, and the Falkland segment. The Moore discontinuity belongs to the Austral segment located within the 25°~27°30′ S area. The Moore and Rio Grande fault zones subdivide the Moore discontinuity into three ridge segments labelled 1 N to 3 N [35]. The development of fault structures and volcanic activity provides conditions for hydrothermal circulation [36]. The Xunmei HF is located in the 2 N ridge segment between 25°40′ and 26°35′. It is approximately 100 km long and represents an asymmetric slow-spreading ridge, with a westward spreading rate of approximately 19.3 mm/yr and an eastward spreading rate of approximately 16.3 mm/yr [35,37]. The Xunmei HF was discovered during cruise DY115-22 in 2011 and reinvestigated during cruise DY135-46 in 2017.

The Xunmei HF is located in a depression between two volcanoes (Figure 1b). At a water depth of approximately 2600 m, a flat plateau has formed along a 7–9 km wide axial valley [37]. The bedrock mainly consists of N-MORB and lesser microcrystalline basalt, vesicular basalt, porous basalt, and basaltic glass [38,39]. The high-elevation fields are completely composed of pillow basalt, with a flat top and limited sedimentation. In the low-elevation fields, fresh basalt is partially covered by loose sediments, whereas no ultramafic rocks are exposed [28]. Abundant metallic sulfide fragments, vent biota, chimney fragments, and inactive chimneys on slopes and low-lying fields were observed by camera tow surveys [40]. The detected temperature anomalies, presence of methane (CH_4), and widespread turbidity anomalies highlight the existence of hydrothermal vents in the Xunmei HF. A recent underwater video survey conducted in the Xunmei HF revealed the presence of three different types of sulfide chimneys. The iron-rich sulfide chimneys were predominantly composed of pyrite and marcasite; the iron-copper-rich sulfide chimneys were mainly composed of pyrite and chalcopyrite; the copper-rich sulfide chimneys were primarily composed of chalcopyrite and pyrite [41].

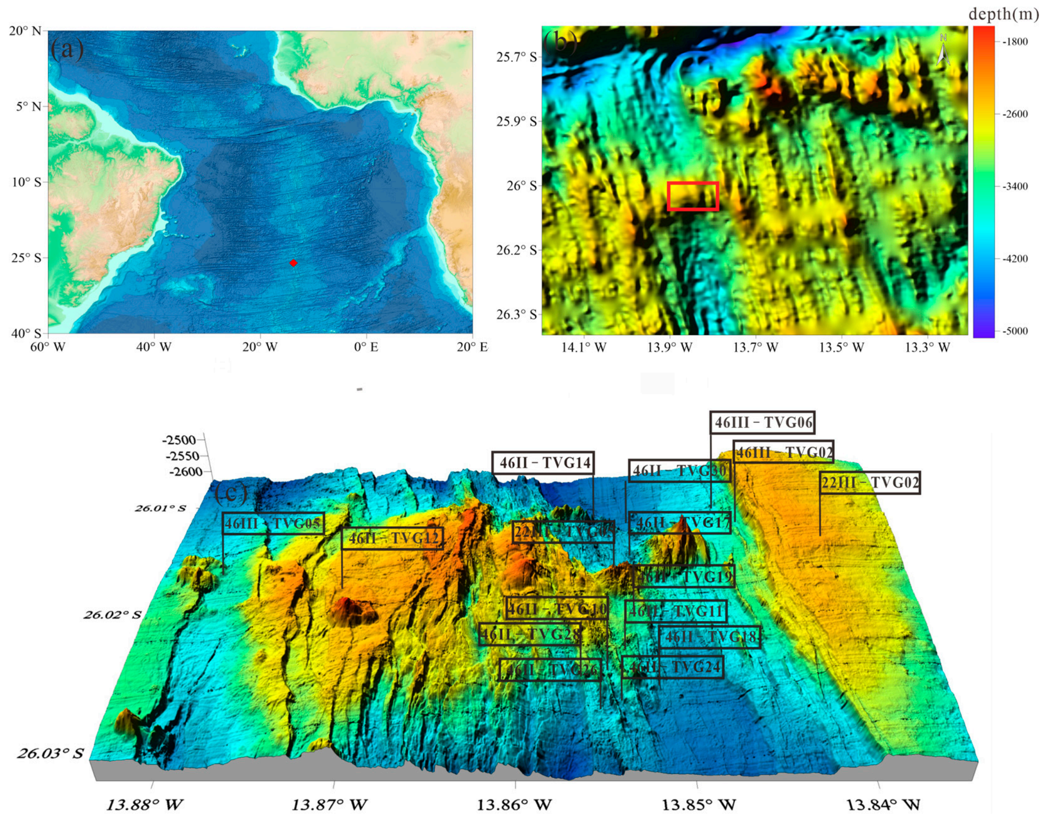

Figure 1. Location and topography of the Xunmei HF. The topographic data in (**a**,**b**) are from www.GEBCO.net (accessed on 8 June 2023), while the data in (**c**) are derived from AUV multibeam bathymetric surveys.

3. Materials and Methods

Since 2009, the China Ocean Association has organized ocean cruises to collect seabed sediment samples at over 70 stations in the SMAR [34]. The seabed sediments used in Xunmei HF (Figure 2) were obtained from segment III of cruise DY115-22 and segments II and III of cruise DY135-46 using a TV grab sampler. A total of 16 seabed sediment samples were collected within the depth range of 2445 to 2595 m (Figure 1c and Table S1). X-ray diffraction (XRD) analysis revealed the presence of sulfides, including pyrite, sphalerite, marcasite, chalcopyrite, and minor goethite and barite [34].

In addition, ten samples were collected at stations relatively far from the HF in the SMAR to represent the mineral compositions and elemental compositions of the background sediments (BGS). Among these samples, the closest distance to a known hydrothermal field is approximately 35 km, other samples were located far from the known vents with a distance between 80 and 500 km. Sediments are light yellow to yellow calcareous containing foraminiferal shells mixed with rock fragments. X-ray diffraction (XRD) analysis indicates that the sediments are mainly composed of calcite, with small amounts of goethite, hematite, and feldspar present in some samples [34].

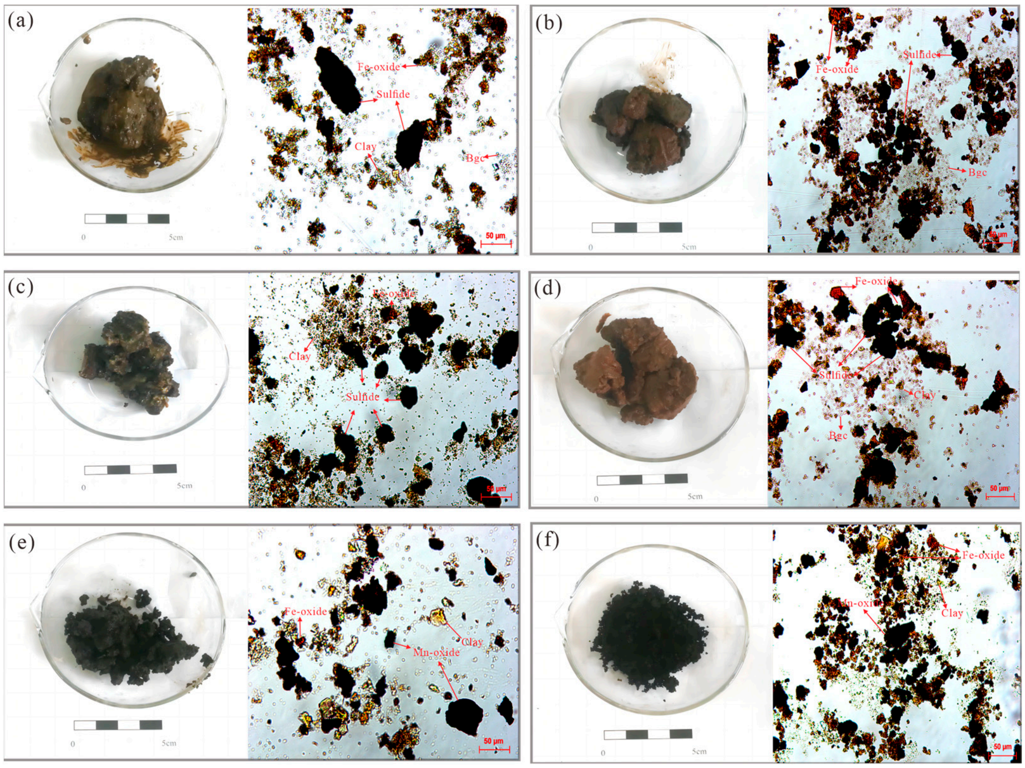

Figure 2. Typical photographs and optical microscope photos of seabed sediments from the study area. 46III-TVG02 (**a**), 46III-TVG06 (**b**), 46II-TVG14 (**c**), and 46II-TVG30 (**d**) hydrothermal sediments with small amounts of sulfide chimney debris; (**e**) 46II-TVG24 and (**f**) 46III-TVG05 hydrothermal sediments enriched in Mn oxides debris. Bgc-Biogenic compositions.

Geochemical analysis was conducted at the Key Laboratory of Marine Geology and Metallogeny, Ministry of Natural Resources, Qingdao, China. The test method follows the methodology of Ref. [34]. The pretreatment method for sediment samples was as follows: first, the powdered sample was dried in an 80 °C oven. Then, 50.00 mg of the sample was placed in a digestion vessel, followed by the addition of 1.50 mL high-purity HNO_3 and 1.50 mL high-purity HF. The mixture was heated to 190 °C for 48 h to decompose. After cooling, it was evaporated to dryness. Then, 1.50 mL HNO_3 was added and evaporated to remove residual HF. For complete digestion, a total of 3.0 mL HNO_3 was added to the solution, which was again heated for 8 h. The clear solution was removed and diluted for analysis. Finally, the sample was heated to 150 °C for 12 h to dissolve. After cooling, the sample was diluted for analysis. The major elements analysis was determined by ICP-OES, and trace and rare earth elements were measured by ICP-MS. The accuracy was controlled for both major and trace elements by measuring the standard reference solutions, Multielement Solution2 (CLMS-2), and the sulfide standard material (CRM) GBW07267, as well as blank and duplicate samples. The relative error was kept below 10%, and the relative standard deviation (RSD) was below 5%.

4. Results

The major and trace element contents are listed in Table 1. The complete geochemical analysis results can be found in Table S1.

Table 1. Major and trace elements of the sediments from Xunmei. Major elements in wt.%, trace elements in μg/g.

Elements	Xunmei (n = 16)					BGS (n = 10)	Basalts (n = 16)	Serpentinite (n = 16)
	Min	Max	Average	Median	SD	Average	Average	Average
Al_2O_3	0.18	11.70	4.60	3.73	4.14	4.27	14.94	1.14
SiO_2	5.94	41.80	24.22	24.90	11.50	13.49	50.81	39.34
CaO	0.33	37.10	10.31	4.61	12.22	38.95	12.00	0.51
Fe_2O_3	6.55	55.50	30.39	29.30	17.68	2.97	9.77	8.64
K_2O	0.12	0.90	0.27	0.17	0.23	0.34	0.11	-
MgO	0.27	6.71	3.02	2.61	2.05	2.32	8.02	37.18
MnO	0.05	31.40	3.76	0.44	9.09	0.15	0.16	0.12
Na_2O	0.62	2.85	1.82	1.86	0.56	1.70	2.54	0.11
P_2O_5	0.20	1.50	0.66	0.70	0.36	0.08	0.09	---
TiO_2	0.01	1.10	0.37	0.31	0.36	0.29	1.28	0.04
Ba	31	1828	297	110	530	225	2.8	-
Sr	11	1268	404	216	406	1251	113	
V	74	806	331	317	190	63	266	39
Zn	184	57,936	6922	3350	14,263	41	72	36
Zr	2.5	57	25	25	20	28	82	
Co	17	305	115	92	73	23	41	90
Cu	806	58,286	16,431	11,514	16,817	56	72	12
Ni	2.9	335	52	36	79	53	71	1947
Cr	16.4	232	101	88	68	65	324	1238
Sc	0.5	34	12	11	11	9	40	
U	0.3	11	4.2	3.7	3.4	0.4	0.1	
Y	0.9	29	14	15	9	14.6	27	
Mo	3	394	122	86	128	1.1	0.5	
Zr	2.5	62	25	25	20	31	82	
Metalliferous Sediment Index (MSI)	0.32	42.08	14.26	10.30	14.33	44.09		
∑REE	1.6	52	28	33	17	50		
LREE	1	38	20	23	13	42		
HREE	0.6	15	8	9	5	8		
L/H	1.5	4.3	3	2.5	0.9	5		
δEu	0.9	4.5	1.6	1	1.1	0.8		
δCe	0.3	0.8	0.6	0.6	0.2	0.7		

4.1. Major Elements

The CaO content of the sediments in Xunmei ranges from 0.33 to 37.10 wt.% (average = 10.31 wt.%), which is significantly lower than the CaO content of the background sediments (BGS: 38.95 wt.%, see Table 1). The contents of Al_2O_3, Fe_2O_3, and MgO range from 0.18 to 11.70 wt.%, 6.55 to 55.50 wt.%, and 0.27 to 6.71 wt.%, respectively, with average values of 4.60 wt.%, 30.39 wt.%, and 3.02 wt.%. The Fe_2O_3 content is significantly higher than that of the BGS, while the Al_2O_3 and MgO contents are relatively similar to those of the BGS. The SiO_2 and TiO_2 contents are also relatively high, ranging from 5.94 to 41.80 wt.% and 0.01 to 1.10 wt.%, respectively. The average contents of K_2O (0.27 wt.%), MgO (3.02 wt.%), and Na_2O (1.82 wt.%) are similar to those of the BGS (0.34 wt.%, 2.32 wt.%, and 1.70 wt.%, respectively). The average contents of MnO (3.76 wt.%) and P_2O_5 (0.66 wt.%) are one order of magnitude higher than those of the BGS (0.15 wt.% and 0.08 wt.%, respectively).

4.2. Trace Elements

The concentrations of Cu and Zn ranged from 806 to 58,286 μg/g and 184 to 57,936 μg/g, with average values of 16,431 μg/g and 6922 μg/g, respectively. These concentrations were significantly higher than those of the BGS, but there were large differences in element concentrations among different samples. The Co concentration was relatively high (17 to 305 μg/g, with an average value of 115 μg/g), which distinguishes those from other hydrothermal fields [6,10,27,42]. Heavy metals such as Cu, Zn, Fe, Mn, and Co in the Xunmei sediments were much higher than those in the BGS (Table 1). In addition, the average Cu/Al, Zn/Al, and Co/Al ratios in the Xunmei sediments (6734, 2837, and 47, respectively) were higher than the average values in the BGS (22, 16, and 9, respectively). The average concentrations of Ni and Cr were 52 μg/g and 101 μg/g, respectively; the Cr contents were slightly higher than those of the BGS (average of 65 μg/g), while the Ni contents were similar to those of the BGS (average of 53 μg/g). Notably, the sediments in Xunmei were significantly enriched in Mo (average of 122 μg/g), V (average of 331 μg/g), and U (average of 4.2 μg/g) compared to the BGS (average of 1.1 μg/g for Mo, 63 μg/g for V and 0.4 μg/g for U).

4.3. Rare Earth Elements

The total contents of rare earth elements (∑REE) range from 1.6 to 52 μg/g. The ratios of light rare earth elements to heavy rare earth elements (LREE/HREE) range from 1.5 to 4.3, indicating enrichment in LREEs (Figure 3a). All sediment samples show negative Ce anomalies (δCe ranges from 0.3 to 0.8, with an average of 0.6). Two types of Eu anomalies are observed in the sediment samples (Figure 3). Among them, samples 22III-TVG02, 46II-TVG10, 46II-TVG11, 46II-TVG12, and 46II-TVG28 exhibit slight negative Eu anomalies, while samples 46II-TVG14 and 46II-TVG24 show strong positive Eu anomalies (Table S1). The BGS-normalized REE patterns (Figure 3b) exhibit more pronounced positive Eu anomalies.

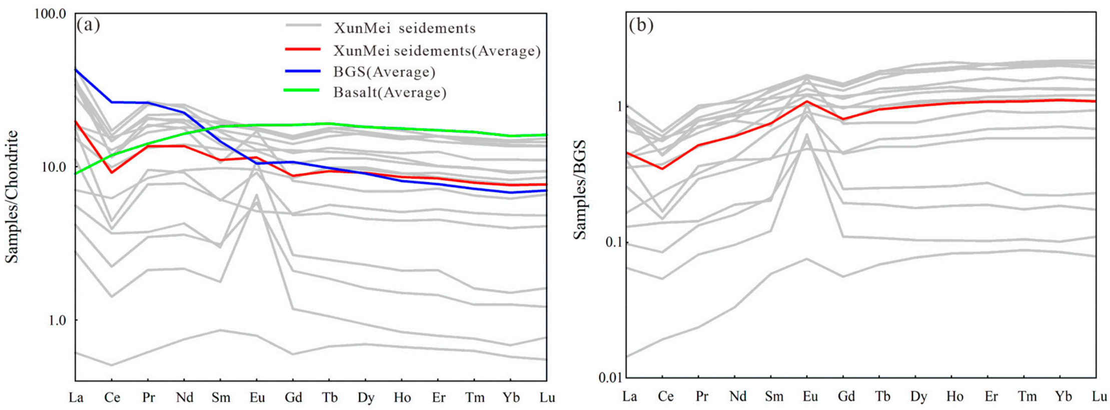

Figure 3. REE pattern normalization of sediments from Xunmei: (**a**) chondrite [43] and (**b**) background sediment (BGS). BGS: see Table S1; basalt: unpublished data (Guan Y).

5. Discussion

5.1. Sediment Compositions

The mid-ocean ridge sediments can be considered a mixture of background pelagic materials (with constant Al/Mg ratios), basaltic or ultramafic debris (with low Al/Mg ratios), iron-manganese oxides, and hydrothermal components (very low Al and Mg content) [6].

Partial principal component analysis (PCA) of the major and trace elements in the Xunmei samples was performed by version IBM SPSS Statistics 23 software (Table S2). Based on the criterion of eigenvalues greater than 1 and after a varimax orthogonal rotation, a total of 4 principal factors were obtained (Table 2). The cumulative variance contribution rate of the 4 principal factors in the Xunmei sediments was close to 96%, therefore effectively representing the characteristics of all analyzed samples. The specific analysis results are as follows: (1) The elements closely related to F1 are Al, Ti, Mg, Sc, and Y, representing the lithogenic components. (2) The elements closely associated with the F2 factor include Mn, Mo, K, and Ba, representing elements scavenged from seawater during the migration process of neutral-buoyancy hydrothermal plumes. (3) In the F3 factor, Fe, Cu, and U are positive loadings, representing Fe oxyhydroxides, hydrothermal Cu, and other nonbuoyant hydrothermal plume particles, while Ca is a negative loading, representing calcium biogenic components [34]. (4) The F4 factor is closely related to Zn and Cu and is primarily associated with sulfides, representing the contribution of sulfide chimney fragments.

Table 2. Results of factor analysis of surface sediments.

	F1	F2	F3	F4
Eigenvalue	7.306	3.615	1.427	1.008
Cumulative%	52.183	78.003	88.196	95.397
Al	0.925	−0.320	−0.160	−0.113
Fe	−0.427	−0.182	0.757	0.354
Mn	−0.110	0.977	−0.062	−0.055
Zn	−0.301	−0.067	0.064	0.935
Cu	−0.119	−0.262	0.566	0.698
Mo	−0.356	0.794	0.420	0.088
U	−0.375	−0.047	0.884	−0.129
Ti	0.925	−0.303	−0.194	−0.091
Mg	0.958	0.002	−0.203	−0.162
K	−0.249	0.926	0.084	−0.148
Sc	0.919	−0.284	−0.236	−0.116
Y	0.794	−0.216	−0.397	−0.309
Ba	−0.176	0.943	−0.146	−0.082
Ca	0.144	−0.331	−0.841	−0.301

Early studies have shown that Al and Ti may represent the detrital components of sediments [44], and they have high concentrations in the Xunmei samples (the average content of Al_2O_3 is 4.60% and that of TiO_2 is 0.37%). On the Al_2O_3-TiO_2 and Al_2O_3-MgO diagrams, both the BGS and the Xunmei sediments are mainly located within the linear range of basalt, indicating that their detrital components mainly originate from basalt. Compared with the other stations, 46II-TVG14, 46II-TVG24, 46II-TVG30, and 46III-TVG05 contain more MgO, but the content is lower than that of serpentinite (Figure 4b). Regardless of the tectonic setting, the content of Mg in hydrothermal fluids is below the detection limit, except for Karei HF (2.5 mM) [45]. The higher MgO contents in the sediments of the Dragon Horn, Saladaha, and Rainbow HFs are due to the presence of a large amount of ultramafic debris [6,24,42], but the basement rocks in the Xunmei field are N-MORB [38], and no ultramafic rocks are exposed. Therefore, the enrichment of MgO cannot originate from the input of ultrabasic rock fragments.

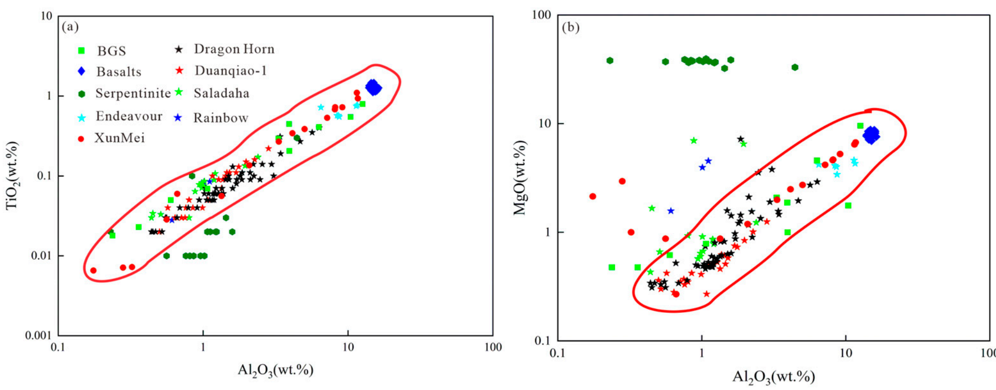

Figure 4. Al_2O_3-TiO_2 (**a**) and Al_2O_3-MgO (**b**) diagrams. Data sources: Endeavour [10]; Dragon Horn [6]; Duanqiao-1 [27]; Saldanha and Rainbow [42]; Serpentinite [46]; Basalt: unpublished data (Guan Y).

Yang et al. [34] utilized geochemical quantification criteria: a Fe content (carbonate-free basis) >10% (without carbonate substrate) and an Al/(|Al + Fe + Mn|) value of <0.4, to distinguish metalliferous and nonmetalliferous sediments. 15 samples were classified as metalliferous sediments. The metalliferous sediment index (MSI = 100 × Al/(|Al + Fe + Mn|)) was used to indicate the degree of metal enrichment in sediments [17]. The MSI of the sediments ranged from a maximum of 42.08% to a minimum of 0.32%, indicating significant metal enrichment in the sediments (see Table S1).

On the Fe-Al-Mg diagram, the BGSs show similarities to the basaltic rocks (Figure 5a). However, the BGSs exhibit higher manganese contents and similar iron contents compared with the basalts (Figure 5b). The BGS locations are far from known hydrothermal fields, therefore it is unlikely that the iron and manganese are associated with hydrothermal sulfides, indicating the presence of iron oxyhydroxides and manganese oxides. The Xunmei sediments are enriched in Cu, Zn, and Fe (Figure 5a–c), suggesting the input of hydrothermal-derived components. Copper, Zn, and Fe are significantly enriched in Xunmei HF compared with other HFs, and their high concentrations are believed to be associated with sulfides [26]. The Xunmei sediments exhibit a Cu-Zn enrichment pattern, which is different from the Fe-Cu enrichment pattern observed in the Duanqiao-1, Dragon Horn, and Endeavour HFs (Figure 5c), suggesting the Xunmei sediments may be closer to the vents. Additionally, the Xunmei sediments have low MSI values. These characteristics indicate a high abundance of hydrothermal components in the sediments.

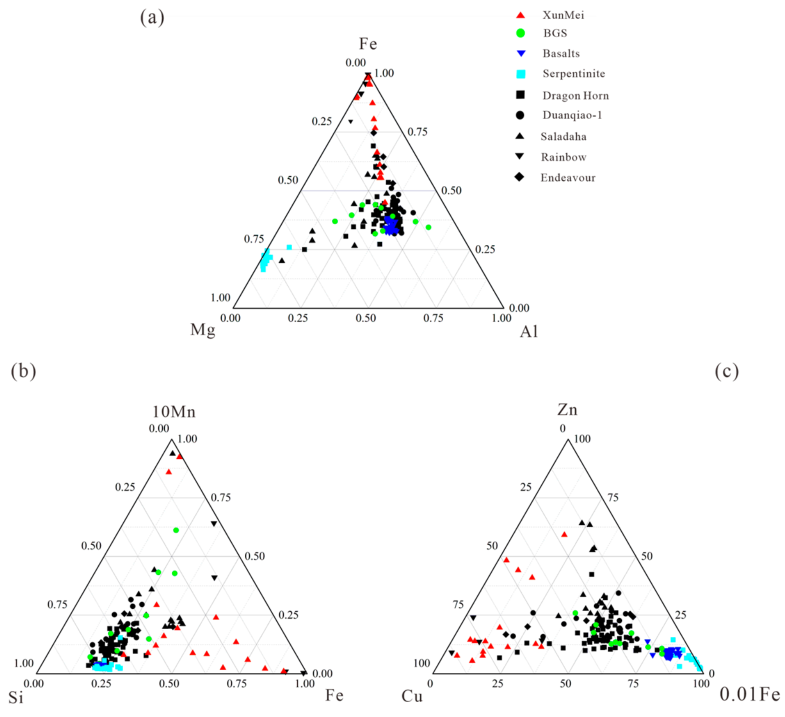

Figure 5. Fe-Al-Mg (**a**), Si-Fe-10Mn (**b**), and Cu-0.01Fe-Zn (**c**) diagrams of sediment compositions. Data source: Same as Figure 4.

On the Si-Fe-10Mn diagram, the majority of the Xunmei sediments plot closer to the Fe apex than basalt, the BGS, and other hydrothermal sediments (Duanqiao-1, Dragon Horn, Saldanha, Rainbow, and Endeavour HFs). Only samples 46II-TVG24 and 46III-TVG05 plot closer to manganese, indicating that the majority of the samples are Fe-rich phase, while the samples 46II-TVG24 and 46III-TVG05 are Mn-rich phase.

Previous studies have shown that hydrothermal fluids in mid-ocean ridges are typically enriched in LREEs, exhibit significant positive Eu anomalies, and lack Ce anomalies [47]. However, sediment samples from the Xunmei HF display two distinct REE patterns (Figure 3): one with a clear positive Eu anomaly, similar to the hydrothermal fluid REE pattern, and another with no Eu anomaly and no negative Ce anomaly. This is interpreted as the occurrence of phase separation in the hydrothermal fluids, resulting in two distinct patterns of REEs (positive Eu anomalies and no Eu anomalies), and the sulfides and sediments also develop REEs patterns similar to hydrothermal fluids [34].

The Fe/Ti vs. Al/(|Al + Fe + Mn|) diagram (Figure 6) illustrates the relative contributions of hydrothermal and detrital components in the seabed sediments. The decrease in Fe/Ti ratios and the increase in Al/(|Al + Fe + Mn|) ratios indicate the dilution of metalliferous sediments by pelagic sediments [42]. The sediment compositions in Xunmei HF fall between the BGS and the metalliferous sediments. In conclusion, the Xunmei sediments can be interpreted as a mixture of BGS, basaltic debris, iron-manganese oxides, and hydrothermal components.

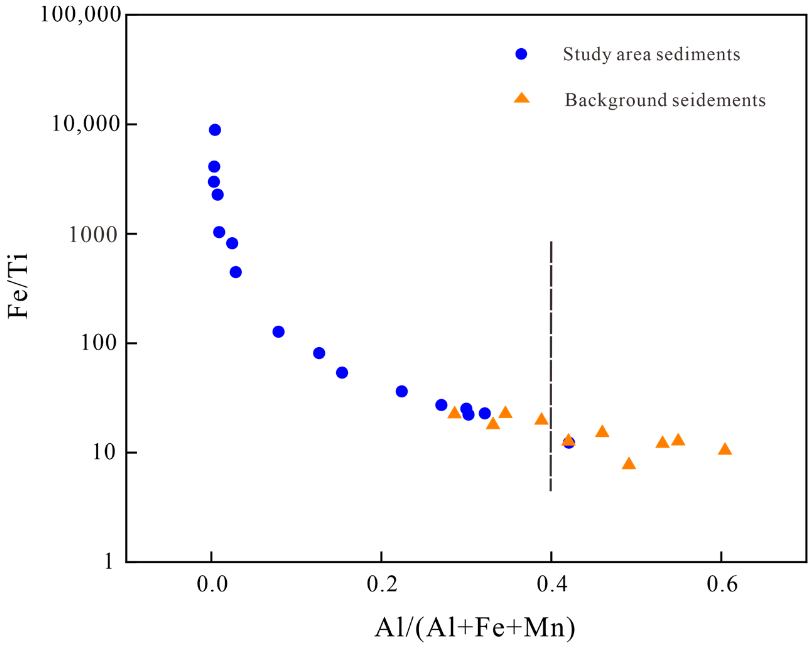

Figure 6. Al/(Al + Fe + Mn) vs. Fe/Ti diagram of Xunmei sediments and background sediments. The dashed line represents the boundary between metalliferous and nonmetalliferous sediments.

5.2. Distribution Characteristics of Hydrothermal-Derived Elements in Sediments

According to the methods proposed by Refs. [6,24], the contribution of each endmember to the sediment composition can be calculated using the following procedure:

The element contents of seabed sediments can be directly obtained through geochemistry. The exposed basement rock in Xunmei is predominantly basalt [38], with significantly higher Al_2O_3 content than ultramafic rocks (Table 1). Therefore, Al in the Xunmei sediments mainly originates from basaltic debris. Therefore, the contents of basaltic debris can be calculated from the formula:

$$\mathrm{Element}_{\mathrm{Basaltic}} = (\mathrm{Element/Al})_{\mathrm{background}} \times \mathrm{Al}_{\mathrm{total.}}$$

$\mathrm{Element}_{\mathrm{Basaltic}}$: the content of element inbasaltic debris; $(\mathrm{Element/Al})_{\mathrm{background}}$: elements/Al in the background sediments; $\mathrm{Al}_{\mathrm{total}}$: the total content of Al in Xunmei sediments.

The iron–manganese oxides in mid-ocean ridge sediments are typically the precipitates of neutral-buoyancy hydrothermal plumes [27]. Therefore, it can be assumed that the residual element abundance, after subtracting the contribution from debris, represents the hydrothermal contribution. The calculation formula is as follows:

$$\mathrm{Element}_{\mathrm{Hydrothermal}} = \mathrm{Element}_{\mathrm{Total}} - \mathrm{Element}_{\mathrm{Basaltic}}.$$

$\mathrm{Element}_{\mathrm{Hydrothermal}}$: the contents of elements derived from hydrothermal processes and their related elements. $\mathrm{Element}_{\mathrm{Total}}$: the total contents of specific elements in the Xunmei sediments. $\mathrm{Element}_{\mathrm{Basaltic}}$: the contents of elements derived from basaltic debris.

The calculation results are shown in Table 3. "---" represents the absence of hydrother mal-derived elements.

Table 3. Calculation results of hydrothermal-derived elements in sediments.

Element (Hydrothermal)	Cu	Fe	Zn	Co	Mn	P	V	Mo	U
	wt.%	wt.%	wt.%	μg/g	wt.%	wt.%	μg/g	μg/g	μg/g
22II-TVG02	0.17	4.30	0.03	28.28	0.19	0.10	119.81	4.29	0.39
22II-TVG05	2.78	19.63	0.51	126.76	0.13	0.21	251.52	54.03	4.77
46II-TVG10	0.51	7.36	0.08	80.21	0.26	0.15	234.08	7.34	0.40
46II-TVG11	0.12	2.83	0.02	---	---	---	139.38	0.40	---
46II-TVG12	0.08	2.67	0.01	37.77	0.35	0.05	90.54	3.93	0.25
46II-TVG14	1.89	38.51	1.80	303.09	0.09	0.34	139.80	76.65	3.41
46II-TVG17	1.62	26.93	0.30	177.33	0.42	0.43	448.82	248.07	11.36
46II-TVG18	0.60	6.71	0.07	94.25	0.12	0.12	216.37	6.30	0.24
46II-TVG19	0.67	7.34	0.06	97.39	0.02	0.10	228.55	18.46	0.07
46II-TVG24	0.13	11.67	0.37	94.81	16.85	0.09	71.64	356.18	3.77
46II-TVG26	2.67	27.22	0.48	171.15	1.18	0.61	570.81	106.03	6.18
46II-TVG28	2.54	35.34	0.17	66.33	0.68	0.35	389.60	210.41	7.51
46II-TVG30	1.71	38.52	0.51	82.10	0.29	0.33	212.41	96.02	8.26
46III-TVG02	5.83	36.69	5.79	13.47	0.03	0.36	203.01	183.67	4.02
46III-TVG05	0.46	17.43	0.44	61.75	24.28	0.38	802.37	395.39	3.52
46III-TVG06	4.43	22.71	0.39	53.47	---	0.37	204.08	162.62	6.62

5.2.1. Cu, Zn, Fe, Co

Previous studies have shown that elements in hydrothermal plumes exhibit three main behaviors compared to the dominant element Fe: (1) Chalcophile elements with preferential removal from the hydrothermal plume due to settling and/or oxidative dissolution of sulfides, (2) elements primarily present in seawater as oxyanions appear to coprecipitate with iron oxyhydroxides in the early stages of hydrothermal plume formation, exhibiting constant ratios with iron, and (3) particle-reactive elements such as Be, Y, Th, and REEs showing increasing elemental ratios with Fe, indicating continuous scavenging from seawater onto precipitated oxyhydroxide particles [48–50].

In the Xunmei sediments, Fe exhibits higher concentrations in the southern and northern areas, while lower concentrations are observed in the central depression. Copper and iron show similar distribution patterns (Figure 7a,b). The higher concentrations in the southern and northern areas indicate that the surface sediments in this field have received more hydrothermal Cu. Additionally, the maturity of chimneys in the southern area and altered secondary minerals in the sediments may also contribute to the enrichment of Cu and Fe. In contrast, Zn shows a different distribution pattern, with the highest concentrations in the northeast and much lower concentrations in other areas (Figure 7c). The highest concentrations of Cu and Zn are both found in the northeast at sample 46III-TVG02. In comparison, Fe exhibits four high concentration centers (46II-TVG14, 46II-TVG28, 46II-TVG30, 46III-TVG02), with the highest values occurring in the northern area (46II-TVG14 and 46II-TVG30). XRD analysis revealed that sample 46III-TVG02 is composed of marcasite, pyrite, sphalerite, and chalcopyrite; samples 46II-TVG28 and 46II-TVG30 contain predominantly pyrite; sample 46II-TVG14 is composed of pyrite, sphalerite, barite and traces of chalcopyrite [34]. Previous studies have shown that Cu, Zn, and Fe are significantly enriched at the source, but compared to Fe, the concentrations of Cu and Zn decrease more rapidly with increasing distance from the vent and are predominantly deposited as sulfides [10,24,27]. In contrast to Cu and Fe, the distribution of Co is relatively uniform, with the highest value occurring in the northern region at sample 46II-TVG14 (Figure 7d). In the Duanqiao-1 HF, Co exhibits two peaks in its lateral distribution, which are interpreted as the early incorporation of Co into the structure of sulfides during the formation of hydrothermal plumes, and the second enrichment is due to the continuous mixing of hydrothermal plumes with seawater, resulting in the scavenging of Co from seawater onto oxides [27]. In the Xunmei HF, Co does not show any significant correlation with other elements (Table 4), suggesting that Co may be enriched from two sources: precipitate from hydrothermal plumes and input of chimney debris.

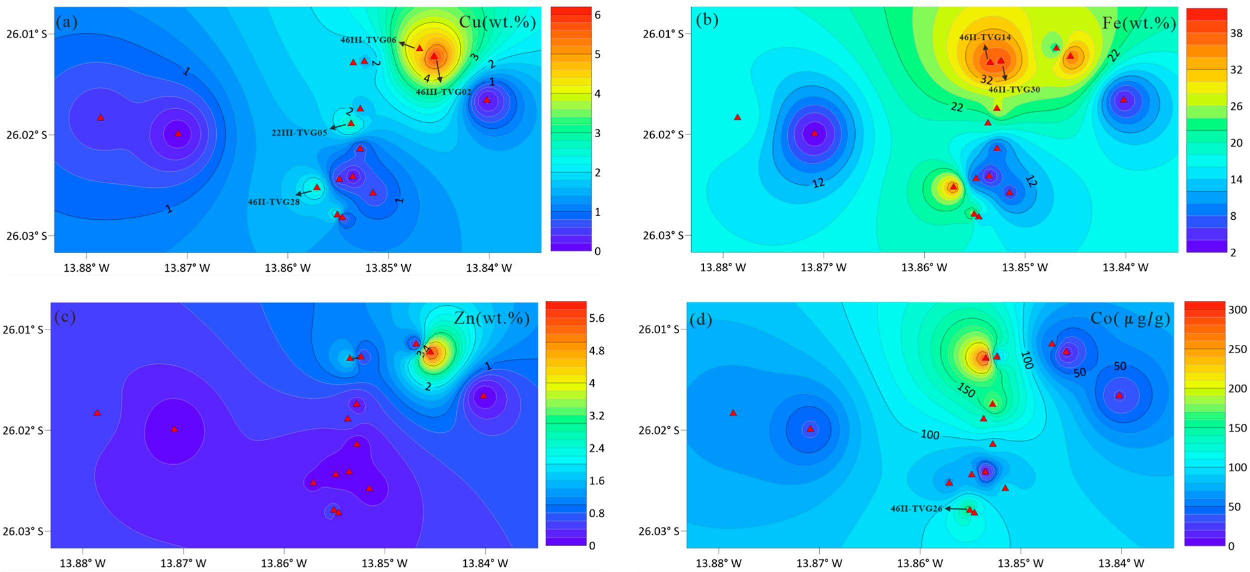

Figure 7. The distributions of hydrothermal-derived elements. (**a**) hydrothermal Cu; (**b**) hydrothermal Fe; (**c**) hydrothermal Zn; (**d**) hydrothermal Co. ▲ represent the station of the sample. X axis-longitude, Y axis-latitude.

Table 4. Correlation analysis of hydrothermal-derived elements of the sediments in the Xunmei HF.

Xunmei		Fe	Mn	Zn	Co	Cu	V	Mo	P	U
Fe	Pearson correlation	1	−0.103	0.523 *	0.308	0.697 **	0.259	0.370	0.782 **	0.760 **
	Significant(bilateral)		0.704	0.038	0.246	0.003	0.332	0.158	0.000	0.001
	N	16	16	16	16	16	16	16	16	16
Mn	Pearson correlation	−0.103	1	−0.083	−0.182	−0.297	0.483	0.781 **	0.055	0.003
	Significant(bilateral)	0.704		0.760	0.501	0.263	0.058	0.000	0.839	0.990
	N	16	16	16	16	16	16	16	16	16
Zn	Pearson correlation	0.523 *	−0.083	1	−0.120	0.713 **	−0.078	0.176	0.301	0.104
	Significant(bilateral)	0.038	0.760		0.659	0.002	0.773	0.515	0.257	0.701
	N	16	16	16	16	16	16	16	16	16
Co	Pearson correlation	0.308	−0.182	−0.120	1	0.003	0.101	−0.105	0.339	0.223
	Significant(bilateral)	0.246	0.501	0.659		0.991	0.711	0.698	0.200	0.407
	N	16	16	16	16	16	16	16	16	16
Cu	Pearson correlation	0.697 **	−0.297	0.713 **	0.003	1	0.082	0.174	0.615 *	0.500 *
	Significant(bilateral)	0.003	0.263	0.002	0.991		0.763	0.520	0.011	0.048
	N	16	16	16	16	16	16	16	16	16
V	Pearson correlation	0.259	0.483	−0.078	0.101	0.082	1	0.532 *	0.665 **	0.401
	Significant(bilateral)	0.332	0.058	0.773	0.711	0.763		0.034	0.005	0.124
	N	16	16	16	16	16	16	16	16	16
Mo	Pearson correlation	0.370	0.781 **	0.176	−0.105	0.174	0.532 *	1	0.449	0.540 *
	Significant(bilateral)	0.158	0.000	0.515	0.698	0.520	0.034		0.081	0.031
	N	16	16	16	16	16	16	16	16	16
P	Pearson correlation	0.782 **	0.055	0.301	0.339	0.615 *	0.665 **	0.449	1	0.764 **
	Significant(bilateral)	0.000	0.839	0.257	0.200	0.011	0.005	0.081		0.001
	N	16	16	16	16	16	16	16	16	16
U	Pearson correlation	0.760 **	0.003	0.104	0.223	0.500 *	0.401	0.540 *	0.764 **	1
	Significant(bilateral)	0.001	0.990	0.701	0.407	0.048	0.124	0.031	0.001	
	N	16	16	16	16	16	16	16	16	16

Note: ** Significant correlation at 0.01 level (bilateral); * Significant correlation at 0.05 level (bilateral).

5.2.2. Mn, V, Mo, U, P

The distribution characteristic of Mn is unique. The highest value of Mn is found in the western area at sample 46III-TVG05, while the second highest value is found in the southern area at sample 46II-TVG24 (Figure 8a). The central area has the lowest content, samples 46III-TVG06 and 46II-TVG11 indicating no Mn input associated with hydrothermal activity. There is no clear correlation between Fe and Mn, suggesting that these two metals and their associated elements (E.g., U, P, and Mo) exist in different stages of sedimentation [26]. Compared to Fe, Mn precipitates relatively at a slower rate, therefore, Mn tends to be slowly removed from hydrothermal plumes in dissolved form and precipitated into sediments throughout the buoyancy and neutral-buoyancy plumes [51,52]. Under reducing conditions, the migration distance of Mn increases. For example, in the Dragon Horn field, Mn precipitates at distances greater than 60 km [6]. The high anomalous values of Mn in sediments from western samples 46III-TVG05 and southern sample 46II-TVG24 suggest the presence of relatively oxidized environments near the Xunmei HF.

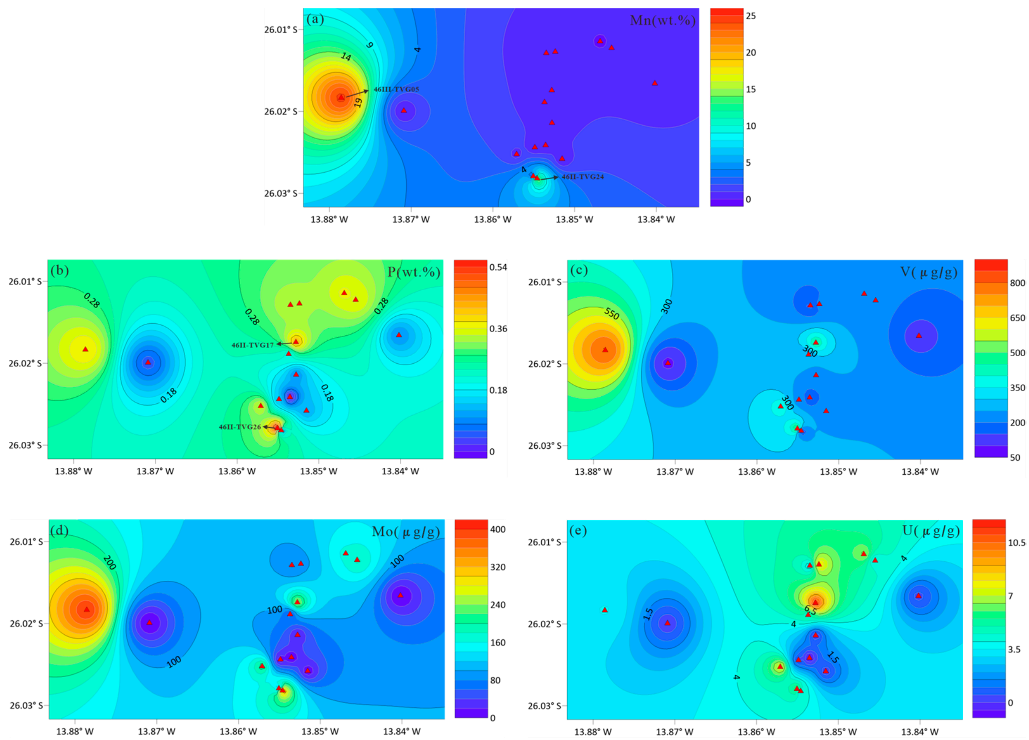

Figure 8. The distributions of hydrothermal-derived elements. (**a**) hydrothermal Mn; (**b**) hydrothermal P; (**c**) hydrothermal V; (**d**) hydrothermal Mo; (**e**) hydrothermal U. ▲ represent the station of sample. X axis-longitude, Y axis-latitude.

The distribution of P is similar to that of Cu and Fe, with higher concentrations in the northern and southern areas and the lowest concentration in the central area. The highest value of P is found in the southern area at sample 46II-TVG26 (Figure 8b). The highest value of V coincides with that of Mn (Figure 8c), but at sample 46II-TVG24, V has the lowest value, while Mn has the second highest value. According to traditional views, V is usually derived from seawater and coprecipitates with oxyhydroxides [50]. It is believed that the P/Fe ratios and V/Fe ratios do not change after the formation of neutral-buoyancy plumes [48,53]. In the Rainbow HF, the P/Fe ratios reported by Edmonds and German [50] remain consistent throughout the hydrothermal plume. The ratios match that of the seabed sediments. On the other hand, the V/Fe ratios gradually increase from the early plume to the sediment. This is consistent with the strong positive correlation observed between P and Fe in Xunmei (R = 0.782, P = 0.000, N = 16), indicating that seawater-derived P coprecipitates with Fe from the hydrothermal plume. The V/Fe ratios in the sediment show significant variability, and V is not significantly correlated with Fe. The anomalous portion of V is mainly derived from sulfides, which have low V/Fe ratios and dilute the primary signal derived from the hydrothermal plume [54].

The high-value fields of Mo are mainly found in western and southern Xunmei (Figure 8d), overlapping with those of Mn, with Mo showing a strong positive correlation with Mn (R = 0.781, P = 0.000, N = 16). Previous studies have suggested that Mo coprecipitates with iron sulfides when reduced to Mo(IV), while Mo(V) and V(IV) are scavenged by oxidized phases in sediments [55]. Therefore, Mo in the Xunmei field is primarily scavenged and coprecipitated with manganese oxides in the form of Mo(V). The distribution pattern of U is similar to that of P, and U showed a strong positive correlation with both P and Fe (U and P, R = 0.764, P = 0.001, N = 16; U and Fe, R = 0.760, P = 0.001, N = 16). It is generally believed that the main source of U in marine metalliferous sediments is seawater and the second source is detrital components (with possible mantle contributions) [10,56,57]. Mills et al. [56] showed that the enrichment of U in iron-capped sediments in the TAG field of the Mid-Atlantic Ridge can be attributed to seawater diffusion into sulfide-derived sediments. In addition to seawater, U in metalliferous sediments has a detrital origin and is associated with clay fractions, phosphates, and organic matter in sediments [57,58]. As shown in Table 1, the U contents in basalt (average of 0.1 μg/g) and the BGS (average of 0.4 μg/g) are low, which does not support a detrital source. Furthermore, the high concentrations of U, Th, Au, Hg, and 3He provide evidence for a mantle source [57]. Apart from U, the remaining elements are not significantly enriched in Xunmei HF, and some are even below the detection limit, thus ruling out a mantle source. Considering the strong positive correlations between U, P, and Fe, the most reasonable source of U is seawater and coprecipitation with hydrothermal Fe.

5.3. Geochemical Characteristics of Hydrothermal Activities in Different Area in Xunmei HF

In Xunmei, the majority of the seabed sediment samples are metalliferous sediments (see Table S1). Although the measured MSI can serve as a useful tracer to indicate the presence of hydrothermal input in deep-sea sediments, it may not provide any effective indication of the distance of that sediment from the source of the hydrothermal input [19]. To discern more "directional" information, different chemical indicators must be utilized. Numerous studies have shown that Cu and Zn are significantly enriched at the vent, primarily distributed in the form of sulfides within a limited distance from the hydrothermal field, and their concentrations decrease significantly with increasing distance from the vent [6,10,24]. However, there is no consensus on the precipitation sequence of different elements, with the focus mainly on the precipitation sequence of Cu and Zn. Mottl and McConachy [51] determined that the enrichment of elements in hydrothermal plumes follows the sequence of Cu, Co, Cd, Zn, Pb, and Ni, while Cave et al. [24] found that, compared to Cu and Fe in the Rainbow HF, Zn preferentially precipitated in the form of sulfides near the vent. Edmonds and German [50] found that chalcophile elements are preferentially removed from hydrothermal fluids in the order of Cd, Zn, Co, and Cu. In the Dragon Horn field, the spatial distribution of hydrothermal Zn is significantly limited compared to that of Cu, occurring only within a range of $\leq$3 km from the hydrothermal vent, indicating that Zn precipitated earlier than Cu from the hydrothermal plume [6]. The Cu/Fe ratios in the Duanqiao-1 HF decrease slightly faster than the Zn/Fe ratios relative to the background value, suggesting that Cu precipitates earlier than Zn [6,27]. The Cu/Fe ratios of the sediments in the Xunmei HF range from 0.012 to 0.195 (Figure 9a), while the Zn/Fe ratios range between 0.005 and 0.158 (Figure 9b). Compared to those of the BGS, the Cu/Fe ratios in the Xunmei sediments are higher by one to two orders of magnitude. The values at samples 22III-TVG05, 46III-TVG06, and 46III-TVG02 are significantly higher than those at the other samples. XRD analysis indicated the presence of sulfides in these samples, including pyrite, sphalerite, chalcopyrite, marcasite, and minor goethite [34]. These findings suggest that as the distance from the vent increases, the Cu/Fe ratios in the sediments decrease significantly. This fractionation is attributed to the preferential settling of sulfide material over low-density oxide material in dispersed neutral-buoyancy plumes [59]. Prior to the discovery of the TAG HF, active vents were believed to be near the eastern wall of the MAR rift at 26° N. Shearme et al. [26] analyzed the core-top geochemical samples that exhibited the highest Cu/Fe ratios and clearly delineated the location of the subsequently discovered TAG hydrothermal mound [60]. Cave et al. [24] confirmed a systematic decrease in Cu/Fe ratios in core-top samples at locations far from the Rainbow HF. Apart from the significantly elevated ratios at sample 46III-TVG02, the differences in the Zn/Fe ratios relative to the BGS were smaller than those in the Cu/Fe ratios. This is attributed to the widespread occurrence of Fe sulfides and Cu-Fe sulfides in the Xunmei HF, where the contents of Zn are low both in sulfides and hydrothermal fluids.

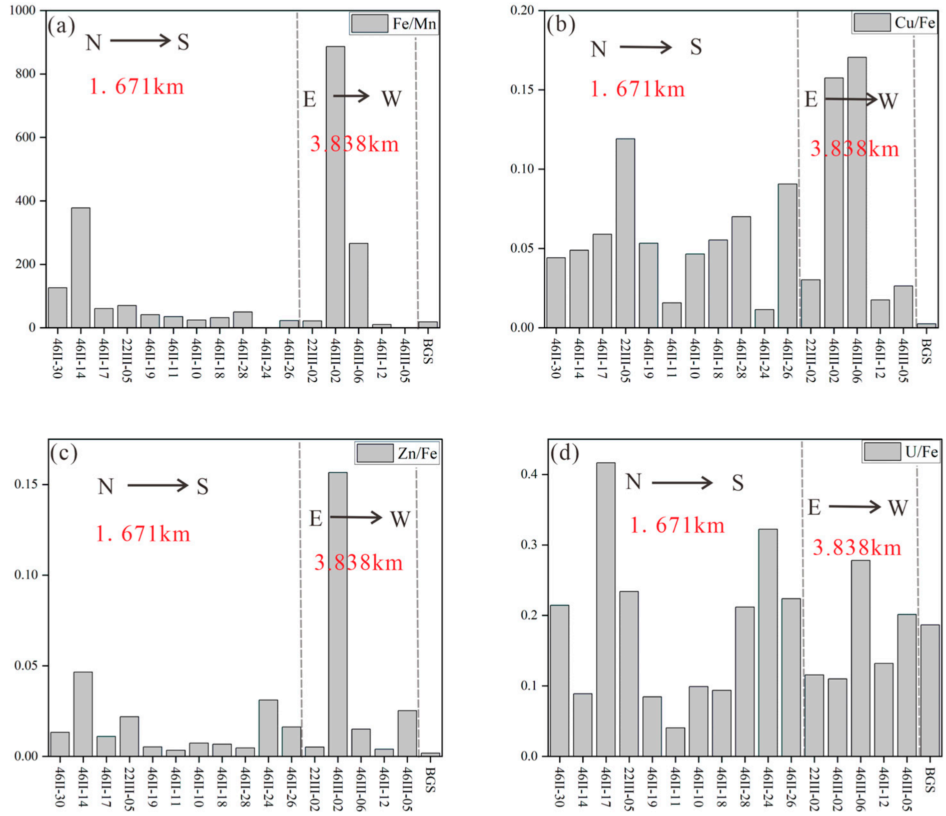

Figure 9. Ratios of Cu/Fe (**a**), Zn/Fe (**b**), Fe/Mn (**c**), and U/Fe (**d**) in sediment derived from hydrothermal activity at different sampling sites. Note: Background values were used for sites without hydrothermal input. N—North, S—South, E—East, W—West. X-axis—sampling location, Y-axis—the numerical value of the ratio.

The dispersion distance of Fe and Mn is much greater than that of Cu and Zn, as previous studies have shown that Fe and Mn in hydrothermal plumes can migrate over long distances and precipitate outside the hydrothermal field in the form of iron and manganese-rich sediments [61], indicating that Fe and Mn can be transported to locations far from the hydrothermal field. Liao et al. [27] found that Fe precipitates in the range of 60 km from the hydrothermal field in the Duanqiao-1 HF, while Mn can disperse to locations beyond 60 km from the field, suggesting that Fe precipitates earlier than Mn. The oxidation rate of Mn in seawater is slower than that of Fe; therefore, it is expected that the Mn/Fe ratios of particles precipitated by hydrothermal plumes will increase with increasing distance from the source [62]. The Fe/Mn ratios in the Xunmei HF range from 0.69 to 1440 (Figure 8c). The Fe/Mn ratios exhibit significant variations, with three samples below the background value and six samples (22III-TVG05, 46II-TVG14, 46II-TVG19, 46II-TVG30, 46III-TVG02, 46III-TVG06) significantly higher than the background value. The remaining samples show ratios similar to the background value. The highest ratio is observed at the northeastern sample 46III-TVG02, reaching a value of 1440. This sample is located within the vicinity of metalliferous sediments near the vent in the Lucky Strike HF (1000–3000), TAG HF (900–2000), OBS HF (900–2400), and Wocan-1 HF (1373–1475) [52,63–65]. Therefore, it can be inferred that this sample is likely proximal to the vent.

Based on the variations in Cu and Zn contents, multiple indicators such as Cu/Fe, Zn/Fe, and Fe/Mn ratios (Figures 7a,c and 9a–c) were used to determine the presence of high-temperature hydrothermal vents near sample 46III-TVG02 in northeastern Xunmei. Previous studies have indicated secondary oxidation of sulfides in hydrothermal environments by the increase in U/Fe ratios in metalliferous sediments [7,56,63–65]. The high concentration of U in hydrothermal sediments is consistent with scavenging from seawater and sulfide oxidation [7,63,64]. The U/Fe ratios (Figure 9d) and the topography of Xunmei indicate that samples located at depressions have higher U/Fe ratios than the background values. Conversely, samples at higher elevations have lower ratios compared to the background values, suggesting higher oxidation rates of sulfides at lower elevations [7,56,63–65]. The U/Fe ratio at sample 46III-TVG02 is lower than the background value, indicating that sulfides at this location have not undergone secondary oxidation and have a lower degree of maturity. The distribution characteristics of metal elements such as Cu, Fe, and Co (Figure 7a,b,d) and elements such as U and P (Figure 8b,e) that are highly correlated with Fe reveal that in addition to the northern Xunmei, the southern part also shows high values of the corresponding elements, indicating the possible presence of hydrothermal vents in southern Xunmei. The distribution range of elements in the southern part is narrower than that in the northern part, indicating that the eruption time of the vents in the southern part was shorter than that in the northern part. Furthermore, investigations have revealed that the chimneys in southern Xunmei show both higher maturity and degree of alteration when compared to those in the northern part, suggesting that the vents in this area may have been inactive for a long time. In the Xunmei HF, western sample 46III-TVG05 and southern sample 46II-TVG24 exhibit significant Mn anomalies. The concentrations of Cu and other metals in these two samples are relatively low, indicating that the high Mn contents cannot be attributed to the collapse of hydrothermal sulfide chimneys. As mentioned earlier, Mn can migrate outside the hydrothermal field, and under reducing conditions, the migration distance can be greater. From the similar distribution patterns of Mn, V, and Mo (Figure 8a,c,d) and the presence of jarosite in clay-sized seabed sediment samples (unpublished data), it can be inferred that there is a relatively oxidizing environment at the edge of the Xunmei field, which is consistent with the high U/Fe ratios in this area.

In summary, there are high-temperature hydrothermal vents located in the northeastern part of the Xunmei HF, while in the southern area, there are inactive vents with shorter eruptive durations. At the edges, a relatively oxidized environment is present.

6. Conclusions

(1) The seabed sediments in Xunmei hydrothermal field are predominantly composed of metalliferous sediments, which are a mixture of background sediments, basalt debris, iron-manganese oxides, and hydrothermal components. These sediments are significantly enriched in Cu, Zn, Fe, and Co derived from hydrothermal vents, as well as elements primarily scavenged from seawater such as Mn, V, Mo, U, and P.

(2) The spatial distribution of hydrothermal elements in sediments exhibits significant variations. The highest concentrations of Cu and Zn are found in the northeastern part of Xunmei, and Fe shows three high-concentration areas in the northeastern, northern, and southern parts of Xunmei. Manganese exhibits abnormally high concentrations in the western and southern parts of Xunmei. U and P primarily coprecipitate with Fe in hydrothermal plumes, and Mo is mainly scavenged by manganese oxides. Vanadium is primarily scavenged by hydrothermal plumes and precipitates to the sediments, and Co primarily originates from the collapse of sulfide chimneys.

(3) Based on the variations in Cu and Zn concentrations, as well as the Cu/Fe, Zn/Fe, and Fe/Mn ratios, high-temperature hydrothermal vents were inferred to exist near sample 46III-TVG02. The distribution patterns of Cu, Fe, Co, and other elements suggest the possible presence of hydrothermal vents in southern Xunmei. The anomalously high values of Mn and the high U/Fe ratios suggest the possible existence of relatively oxidized environments in southern Xunmei.

Future geochemical investigations on sediment core samples are essential to better understand the evolution of the hydrothermal process in the Xunmei HF.

Supplementary Materials: The following supporting information can be downloaded at: https://www.mdpi.com/article/10.3390/min14010107/s1, Table S1: Major and trace element compositions of the bulk sediment of the Xunmei hydrothermal field; Table S2: Partial principal component analysis (PCA) of the major and trace elements in the sediment samples from Xunmei.

Author Contributions: C.L. collected the samples and conceived designed and funded the study; P.Y. wrote the first draft (with contributions from all other co-authors); B.Y. analyzed the major and trace elements of bulk samples; L.F. and D.D. co-supervised the project; Y.G. supplied the data of basalts; Q.Z. designed the bathymetric map; Y.D. co-supervised the project and funded the study. All authors have read and agreed to the published version of the manuscript.

Funding: This study was financially supported by the Basic Scientific Fund for National Public Research Institutes of China (No. 2021Q01), the National Natural Science Foundation of China (No. 42006180, No. 42276080), and the China Ocean Mineral Resources R&D Association (No. DY135-S2-2).

Data Availability Statement: Data are contained within the article and Supplementary Materials.

Acknowledgments: The authors sincerely appreciate the captains and crew of R/V Dayangyihao (DY 22nd) and R/V Xiangyanghong01 (DY 46th) for their immense support during the investigations and sampling of the Xunmei hydrothermal field.

Conflicts of Interest: The authors declare no conflicts of interest.

References

1. Hannington, M.; Jamieson, J.; Monecke, T.; Petersen, S.; Beaulieu, S. The abundance of seafloor massive sulfide deposits. *Geology* **2011**, *39*, 1155–1158. [CrossRef]
2. Luo, H.; Han, X.; Wang, Y.; Wu, X.; Cai, Y.; Yang, M. Exploring the Mechanism and Resource Prospects of Strategic Metal Enrichment in Global Modern Seafloor Massive Sulfides. *Earth Sci. J. China Univ. Geosci.* **2021**, *46*, 3123–3138. [CrossRef]
3. Tao, C.; Li, H.; Yang, Y.; Ni, J.; Cui, R.; Chen, Y.; Li, J.; He, Y.; Huang, W.; Lei, J.; et al. Two hydrothermal fields found on the Southern Mid-Atlantic Ridge. *Sci. China Earth Sci.* **2011**, *54*, 1302–1303. [CrossRef]
4. Tao, C.; Li, H.; Jin, X.; Zhou, J.; Wu, T.; He, Y.; Deng, X.; Gu, C.; Zhang, G.; Liu, W. Seafloor hydrothermal activity and polymetallic sulfide exploration on the southwest Indian ridge. *Chin. Sci. Bull.* **2014**, *59*, 2266–2276. [CrossRef]
5. Chen, S.; Tao, C.; Zhou, J.; Zhang, G.; Qin, H.; Wang, Y.; Chen, D. Distribution characteristics of hydrothermal plumes on the mid-ocean ridge and their indicative role in polymetallic sulfide exploration. *Acta Oceanol. Sin.* **2019**, *41*, 1–12. [CrossRef]
6. Liao, S.; Tao, C.; Li, H.; Zhang, G.; Liang, J.; Yang, W.; Wang, Y. Surface sediment geochemistry and hydrothermal activity indicators in the Dragon Horn area on the Southwest Indian Ridge. *Mar. Geol.* **2018**, *398*, 22–34. [CrossRef]
7. Gurvich, E.G. *Metalliferous Sediments of the World Ocean: Fundamental Theory of Deep Sea Hydrothermal Sedimentation*; Springer: Berlin/Heidelberg, Germany, 2006.
8. Dymond, J.; Corliss, J.B.; Heath, G.R.; Field, C.W.; Dasch, E.J.; Veeh, H.H. Origin of Metalliferous Sediments from the Pacific Ocean. *Geol. Soc. Am. Bull.* **1973**, *84*, 3355–3372. [CrossRef]
9. Mills, R.; Elderfield, H.; Thomson, J. A dual origin for the hydrothermal component in a metalliferous sediment core from the Mid-Atlantic Ridge. *J. Geophys. Res.* **1993**, *98*, 9671–9681. [CrossRef]
10. Hrischeva, E.; Scott, S.D. Geochemistry and morphology of metalliferous sediments and oxyhydroxides from the Endeavour segment, Juan de Fuca Ridge. *Geochim. Cosmochim. Acta* **2007**, *71*, 3476–3497. [CrossRef]
11. Bodeï, S.; Buatier, M.; Steinmann, M.; Adatte, T.; Wheat, C.G. Characterization of metalliferous sediment from a low-temperature hydrothermal environment on the Eastern Flank of the East Pacific Rise. *Mar. Geol.* **2008**, *250*, 128–141. [CrossRef]
12. Dekov, V.M.; Cuadros, J.; Kamenov, G.D.; Weiss, D.; Arnold, T.; Basak, C.; Rochette, P. Metalliferous sediments from the H.M.S. Challenger voyage (1872–1876). *Geochim. Cosmochim. Acta* **2010**, *74*, 5019–5038. [CrossRef]
13. Feely, R.A.; Lewison, M.; Massoth, G.J.; Robert-Baldo, G.; Lavelle, J.W.; Byrne, R.H.; Von Damm, K.L.; Curl, H.C. Composition and dissolution of black smoker particulates from active vents on the Juan de Fuca Ridge. *J. Geophys. Res. Solid Earth* **1987**, *92*, 11347–11363. [CrossRef]

14. Blanc, G.; Anschutz, P.; Pierret, M.-C. Metalliferous sedimentation in the Atlantis II Deep: A geochemical insight. In *Sedimentation and Tectonics in Rift Basins Red Sea Gulf of Aden*; Purser, B.H., Bosence, D.W.J., Eds.; Springer: Dordrecht, The Netherlands, 1998; pp. 505–520.
15. Feely, R.A.; Massoth, G.J.; Baker, E.T.; Lebon, G.T.; Geiselman, T.L. Tracking the dispersal of hydrothermal plumes from the Juan de Fuca Ridge using suspended matter compositions. *J. Geophys. Res. Solid Earth* **1992**, *97*, 3457–3468. [CrossRef]
16. Boström, K.; Kraemer, T.; Gartner, S. Provenance and accumulation rates of opaline silica, Al, Ti, Fe, Mn, Cu, Ni and Co in Pacific pelagic sediments. *Chem. Geol.* **1973**, *11*, 123–148. [CrossRef]
17. Boström, K.; Peterson, M.N.A.; Joensuu, O.; Fisher, D.E. Aluminum-poor ferromanganoan sediments on active oceanic ridges. *J. Geophys. Res.* **1969**, *74*, 3261–3270. [CrossRef]
18. Barrett, T.J.; Jarvis, I.; Hannington, M.D.; Thirlwall, M.F. Chemical characteristics of modern deep-sea metalliferous sediments in closed versus open basins, with emphasis on rare-earth elements and Nd isotopes. *Earth Sci. Rev.* **2021**, *222*, 103801. [CrossRef]
19. German, C.R. Hydrothermal activity on the eastern SWIR (50°–70° E): Evidence from core-top geochemistry, 1887 and 1998. *Geochem. Geophys. Geosystems* **2003**, *4*. [CrossRef]
20. Yu, Z.; Li, H.; Li, M.; Zhai, S. Hydrothermal signature in the axial-sediments from the Carlsberg Ridge in the northwest Indian Ocean. *J. Mar. Syst.* **2018**, *180*, 173–181. [CrossRef]
21. Yang, B.; Liu, J.; Shi, X.; Zhang, H.; Wang, X.; Wu, Y.; Fang, X. Mineralogy and sulfur isotope characteristics of metalliferous sediments from the Tangyin hydrothermal field in the southern Okinawa Trough. *Ore Geol. Rev.* **2020**, *120*, 103464. [CrossRef]
22. Yang, B.; Wu, Y.; Wang, X.; Zhang, Y.; Cui, J.; Yu, M.; Dang, Y.; Shi, X.; Liu, J. Mineralogical and geochemical characteristics and ore-forming mechanism of hydrothermal sediments in the middle and southern Okinawa Trough. *Mar. Geol.* **2021**, *437*, 106501. [CrossRef]
23. Kuhn, T.; Burger, H.; Castradori, D.; Halbach, P. Volcanic and hydrothermal history of ridge segments near the Rodrigues Triple Junction (Central Indian Ocean) deduced from sediment geochemistry. *Mar. Geol.* **2000**, *169*, 391–409. [CrossRef]
24. Cave, R.R.; German, C.R.; Thomson, J.; Nesbitt, R.W. Fluxes to sediments underlying the Rainbow hydrothermal plume at 36°14′N on the Mid-Atlantic Ridge. *Geochim. Cosmochim. Acta* **2002**, *66*, 1905–1923. [CrossRef]
25. Qiu, Z.; Han, X.; Li, M.; Wang, Y.; Chen, X.; Fan, W.; Zhou, Y.; Cui, R.; Wang, L. The temporal variability of hydrothermal activity of Wocan hydrothermal field, Carlsberg Ridge, northwest Indian Ocean. *Ore Geol. Rev.* **2021**, *132*, 103999. [CrossRef]
26. Shearme, S.; Cronan, D.S.; Rona, P.A. Geochemistry of sediments from the TAG Hydrothermal Field, M.A.R. at latitude 26° N. *Mar. Geol.* **1983**, *51*, 269–291. [CrossRef]
27. Liao, S.; Tao, C.; Dias, Á.A.; Su, X.; Yang, Z.; Ni, J.; Liang, J.; Yang, W.; Liu, J.; Li, W.; et al. Surface sediment composition and distribution of hydrothermal derived elements at the Duanqiao-1 hydrothermal field, Southwest Indian Ridge. *Mar. Geol.* **2019**, *416*, 105975. [CrossRef]
28. Fan, L.; Wang, G.; Holzheid, A.; Zoheir, B.; Shi, X. Isocubanite-chalcopyrite intergrowths in the Mid-Atlantic Ridge 26°S hydrothermal vent sulfides. *Geochemistry* **2021**, *81*, 125795. [CrossRef]
29. Fan, L.; Wang, G.; Holzheid, A.; Zoheir, B.; Shi, X. Sulfur and copper isotopic composition of seafloor massive sulfides and fluid evolution in the 26°S hydrothermal field, Southern Mid-Atlantic Ridge. *Mar. Geol.* **2021**, *435*, 106436. [CrossRef]
30. Fan, L.; Wang, G.; Holzheid, A.; Zoheir, B.; Shi, X.; Lei, Q. Systematic variations in trace element composition of pyrites from the 26°S hydrothermal field, Mid-Atlantic Ridge. *Ore Geol. Rev.* **2022**, *148*, 105006. [CrossRef]
31. Wang, S.; Li, C.; Li, B.; Dang, Y.; Ye, J.; Zhu, Z.; Zhang, L.; Shi, X. Constraints on fluid evolution and growth processes of black smoker chimneys by pyrite geochemistry: A case study of the Tongguan hydrothermal field, South Mid-Atlantic Ridge. *Ore Geol. Rev.* **2022**, *140*, 104410. [CrossRef]
32. Wang, S.; Sun, W.; Huang, J.; Zhai, S.; Li, H. Coupled Fe-S isotope composition of sulfide chimneys dominated by temperature heterogeneity in seafloor hydrothermal systems. *Sci. Bull.* **2020**, *65*, 1767–1774. [CrossRef]
33. Tao, C.; Chen, S.; Baker, E.T.; Li, H.; Liang, J.; Liao, S.; Chen, Y.J.; Deng, X.; Zhang, G.; Gu, C.; et al. Hydrothermal plume mapping as a prospecting tool for seafloor sulfide deposits: A case study at the Zouyu-1 and Zouyu-2 hydrothermal fields in the southern Mid-Atlantic Ridge. *Mar. Geophys. Res.* **2017**, *38*, 3–16. [CrossRef]
34. Yang, B.; Liu, J.; Li, C.; Zhu, A.; Wang, H.; Cui, J.; Zhang, H.; Hu, Q.; Shi, X. Mineralogical and geochemical characteristics of near-vent metalliferous sediments: Implications for hydrothermal processes along the southern Mid-Atlantic ridge (12°S–28°S). *Ore Geol. Rev.* **2022**, *148*, 105003. [CrossRef]
35. Carbotte, S.; Welch, S.M.; MacDonald, K.C. Spreading rates, rift propagation, and fracture zone offset histories during the past 5 my on the Mid-Atlantic Ridge; 25°–27°30′ S and 31°–34°30′ S. *Mar. Geophys. Res.* **1991**, *13*, 51–80. [CrossRef]
36. James, R.H.; Elderfield, H. Chemistry of ore-forming fluids and mineral formation rates in an active hydrothermal sulfide deposit on the Mid-Atlantic Ridge. *Geology* **1996**, *24*, 1147–1150. [CrossRef]
37. Niu, Y.; Batiza, R. Magmatic processes at a slow spreading ridge segment: 26°S Mid-Atlantic Ridge. *J. Geophys. Res. Solid Earth* **1994**, *99*, 19719–19740. [CrossRef]
38. Regelous, M.; Niu, Y.; Abouchami, W.; Castillo, P.R. Shallow origin for South Atlantic Dupal Anomaly from lower continental crust: Geochemical evidence from the Mid-Atlantic Ridge at 26°S. *Lithos* **2009**, *112*, 57–72. [CrossRef]
39. Fan, L.; Wang, G.; Shi, X.; Yang, Y.; Holzheid, A.; Zoheir, B.A. Geochemical characteristics and mantle source properties of basalt from the hydrothermal field along the Mid-Atlantic Ridge at 26°S. *Minerol. Petrol.* **2020**, *40*, 9–20.
40. Li, T.; Yang, Y.; Wang, G.; Fan, L.; Wang, C.; Li, B. The Mineralogical Characteristics of Pyrite at 26°S Hydrothermal Field, South Mid-Atlantic Ridge. *Acta Geol. Sin. Engl. Ed.* **2014**, *88*, 179–180. [CrossRef]

41. Shao, M.; Yang, Y.; Su, X.; Ye, J.; Shi, X. Mineralogical Study of Chimneys in the Southern Mid-Atlantic Ridge at 26°S. *China Min. Mag.* **2014**, *23*, 77–81.
42. Dias, Á.S.; Barriga, F.J.A.S. Mineralogy and geochemistry of hydrothermal sediments from the serpentinite-hosted Saldanha hydrothermal field (36°34′ N; 33°26′ W) at MAR. *Mar. Geol.* **2006**, *225*, 157–175. [CrossRef]
43. Sun, S.-s.; McDonough, W.F. Chemical and isotopic systematics of oceanic basalts: Implications for mantle composition and processes. *Geol. Soc. Lond. Spec. Publ.* **1989**, *42*, 313–345. [CrossRef]
44. Bloemsma, M.R.; Zabel, M.; Stuut, J.B.W.; Tjallingii, R.; Collins, J.A.; Weltje, G.J. Modelling the joint variability of grain size and chemical composition in sediments. *Sediment. Geol.* **2012**, *280*, 135–148. [CrossRef]
45. Hannington, M.D.; De Ronde, C.E.J.; Petersen, S.; Hedenquist, J.W.; Thompson, J.F.H.; Goldfarb, R.J.; Richards, J.P. Sea-Floor Tectonics and Submarine Hydrothermal Systems. In *One Hundredth Anniversary Volume*; Society of Economic Geologists: Littleton, CO, USA, 2005.
46. Whattam, S.A.; Früh-Green, G.L.; Cannat, M.; De Hoog, J.C.M.; Schwarzenbach, E.M.; Escartin, J.; John, B.E.; Leybourne, M.I.; Williams, M.J.; Rouméjon, S.; et al. Geochemistry of serpentinized and multiphase altered Atlantis Massif peridotites (IODP Expedition 357): Petrogenesis and discrimination of melt-rock vs. fluid-rock processes. *Chem. Geol.* **2022**, *594*, 120681. [CrossRef]
47. Mills, R.A.; Elderfield, H. Hydrothermal Activity and the Geochemistry of Metalliferous Sediment. *Geophys. Monogr. Ser.* **1995**, *91*, 392–407.
48. Feely, R.A.; Trefry, J.H.; Lebon, G.T.; German, C.R. The relationship between P/Fe and V/Fe ratios in hydrothermal precipitates and dissolved phosphate in seawater. *Geophys. Res. Lett.* **1998**, *25*, 2253–2256. [CrossRef]
49. German, C.R.; Campbell, A.C.; Edmond, J.M. Hydrothermal scavenging at the Mid-Atlantic Ridge: Modification of trace element dissolved fluxes. *Earth Planet. Sci. Lett.* **1991**, *107*, 101–114. [CrossRef]
50. Edmonds, H.N.; German, C.R. Particle geochemistry in the Rainbow hydrothermal plume, Mid-Atlantic Ridge. *Geochim. Cosmochim. Acta* **2004**, *68*, 759–772. [CrossRef]
51. Mottl, M.J.; McConachy, T.F. Chemical processes in buoyant hydrothermal plumes on the East Pacific Rise near 21°N. *Geochim. Cosmochim. Acta* **1990**, *54*, 1911–1927. [CrossRef]
52. German, C.R.; Hergt, J.; Palmer, M.R.; Edmond, J.M. Geochemistry of a hydrothermal sediment core from the OBS vent-field, 21°N East Pacific Rise. *Chem. Geol.* **1999**, *155*, 65–75. [CrossRef]
53. Metz, S.; Trefry, J.H. Field and laboratory studies of metal uptake and release by hydrothermal precipitates. *J. Geophys. Res. Solid Earth* **1993**, *98*, 9661–9666. [CrossRef]
54. Mills, R.A.; Elderfield, H. Rare earth element geochemistry of hydrothermal deposits from the active TAG Mound, 26°N Mid-Atlantic Ridge. *Geochim. Cosmochim. Acta* **1995**, *59*, 3511–3524. [CrossRef]
55. Emerson, S.R.; Huested, S.S. Ocean anoxia and the concentrations of molybdenum and vanadium in seawater. *Mar. Chem.* **1991**, *34*, 177–196. [CrossRef]
56. Mills, R.A.; Thomson, J.; Elderfield, H.; Hinton, R.W.; Hyslop, E. Uranium enrichment in metalliferous sediments from the Mid-Atlantic Ridge. *Earth Planet. Sci. Lett.* **1994**, *124*, 35–47. [CrossRef]
57. Ayupova, N.R.; Melekestseva, I.Y.; Maslennikov, V.V.; Tseluyko, A.S.; Blinov, I.A.; Beltenev, V.E. Uranium accumulation in modern and ancient Fe-oxide sediments: Examples from the Ashadze-2 hydrothermal sulfide field (Mid-Atlantic Ridge) and Yubileynoe massive sulfide deposit (South Urals, Russia). *Sediment. Geol.* **2018**, *367*, 164–174. [CrossRef]
58. Hein, J.R.; Clague, D.A.; Koski, R.A.; Embley, R.W.; Dunham, R.E. Metalliferous Sediment and a Silica-Hematite Deposit within the Blanco Fracture Zone, Northeast Pacific. *Mar. Georesour. Geotechnol.* **2008**, *26*, 317–339. [CrossRef]
59. Trefry, J.H.; Trocine, R.P.; Klinkhammer, G.P.; Rona, P.A. Iron and copper enrichment of suspended particles in dispersed hydrothermal plumes along the mid-Atlantic Ridge. *Geophys. Res. Lett.* **1985**, *12*, 506–509. [CrossRef]
60. Rona, P.A.; Klinkhammer, G.; Nelsen, T.A.; Trefry, J.H.; Elderfield, H. Black smokers, massive sulphides and vent biota at the Mid-Atlantic Ridge. *Nature* **1986**, *321*, 33–37. [CrossRef]
61. Rusakov, V.Y.; Shilov, V.V.; Ryzhenko, B.N.; Gablina, I.F.; Roshchina, I.A.; Kuz'mina, T.G.; Kononkova, N.N.; Dobretsova, I.G. Mineralogical and geochemical zoning of sediments at the Semenov cluster of hydrothermal fields, 13°31′–13°30′ N, Mid-Atlantic Ridge. *Geochem. Int.* **2013**, *51*, 646–669. [CrossRef]
62. Cowen, J.P.; Massoth, G.J.; Feely, R.A. Scavenging rates of dissolved manganese in a hydrothermal vent plume. *Deep Sea Res. Part A Oceanogr. Res. Pap.* **1990**, *37*, 1619–1637. [CrossRef]
63. German, C.R.; Higgs, N.C.; Thomson, J.; Mills, R.; Elderfield, H.; Blusztajn, J.; Fleer, A.P.; Bacon, M.P. A geochemical study of metalliferous sediment from the TAG Hydrothermal Mound, 26°08′ N, Mid-Atlantic Ridge. *J. Geophys. Res.* **1993**, *98*, 9683–9692. [CrossRef]
64. Dias, Á.S.; Mills, R.A.; Taylor, R.N.; Ferreira, P.; Barriga, F.J.A.S. Geochemistry of a sediment push-core from the Lucky Strike hydrothermal field, Mid-Atlantic Ridge. *Chem. Geol.* **2008**, *247*, 339–351. [CrossRef]
65. Popoola, S.O.; Han, X.; Wang, Y.; Qiu, Z.; Ye, Y.; Cai, Y. Mineralogical and Geochemical Signatures of Metalliferous Sediments in Wocan-1 and Wocan-2 Hydrothermal Sites on the Carlsberg Ridge, Indian Ocean. *Minerals* **2019**, *9*, 26. [CrossRef]